Electronic Supplementary Material (ESI) for Journal of Materials Chemistry A.

Supporting Information

Interfacial stability and ionic conductivity enhanced by dopant segregation in eutectic ceramics: the role of Gd segregation in doped CeO_2/CoO and CeO_2/NiO interfaces

Alodia Orera,[a] Funing Wang,[b,c] Elías Ferreiro-Vild,[d] Sonia Serrano-Zabaleta,[a] Aitor Larrañaga,[e] Miguel A. Laguna-Bercero,[a] Elizabeth C. Dickey,[f] Francisco Rivadulla,[d] M. Carmen Muñoz,[c] and Ángel Larrea[a]

[a] Instituto de Ciencia de Materiales de Aragón, CSIC – U. Zaragoza, c/ María de Luna 3, E-50.018 Zaragoza, Spain.
[b] Instituto de Ciencia de Materiales de Madrid, ICMM-CSIC, Cantoblanco, E-28049 Madrid, Spain.
Prof. E.C. Dickey
[c] School of Physics, Shandong University, Jinan 250100, People's Republic of China
[d] CiQUS, Centro de Investigación en Química Biolóxica e Materiais Moleculares, Universidade de Santiago de Compostela, Santiago de Compostela 15782, Spain
[e] SGIker, Servicios Generales de Investigación, Universidad del País Vasco (UPV/EHU), 48080 Bilbao, Spain.
[f] Department of Materials Science & Engineering, North Carolina State University, Raleigh, NC 27695-7907, USA

E-mail: alarrea@unizar.es

1.- Experimental methods

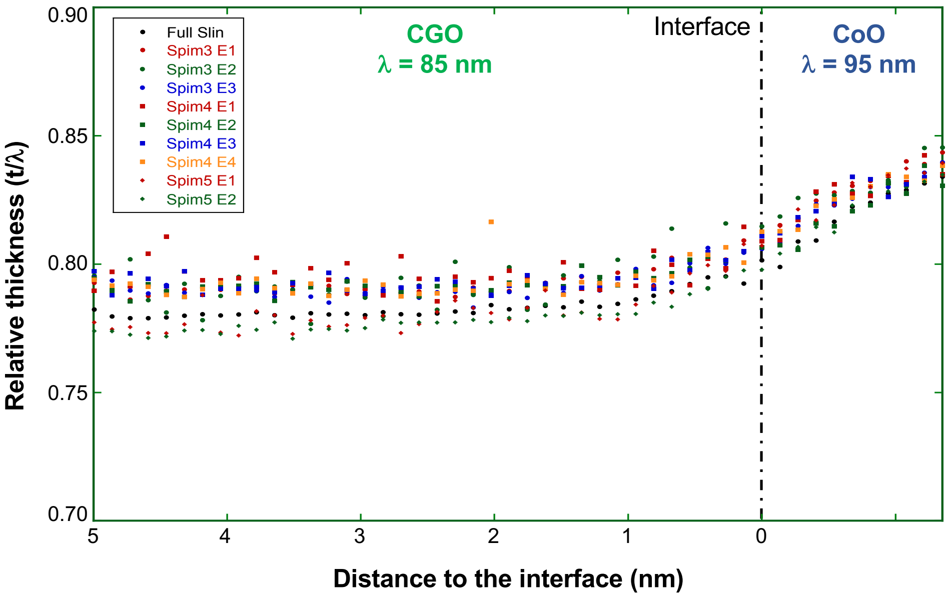

Fig. S1. Three EEL spectrum images were segmented into 9 different subregions with no interfacial steps inside for analysis. Then, the spectrum-images extracted from each subregion were projected along the direction parallel to the interface to obtain a line-trace with accumulated EEL spectra. In this figure we show the relative thickness of the 9 different line-traces, as well as that of the accumulated final line-trace (also included in the figure as Full Slin). The CoO region is slightly thicker due to differential polishing.

2.- Additional experimental results

2.1.- *EBSD estimations of the angle between the actual interface plane and the crystallographic planes.*

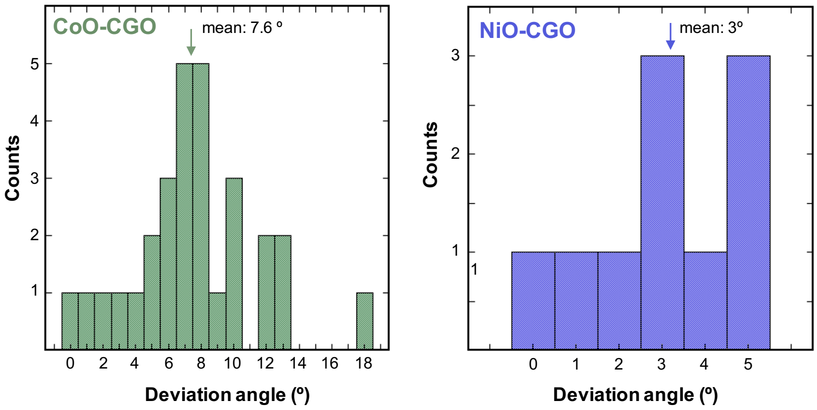

Fig. S2. Due to the formation of terraces along the interface, there is some misorientation between the actual interface plane and the crystallographic interfacial planes, $(001)_{CGO}//(111)_{NiO\text{-}CoO}$. To estimate this angle, we carried out EBSD measurements in different regions. The frequency distribution of the angle measured is represented in this figure. There is good agreement between the measured mean angles, 7.6° and 3° for CoO-CGO and NiO-CGO respectively, and the theoretical estimation discussed in the paper, 7° and 5° respectively.

2.2.- *High resolution images of the CGO-NiO interfaces*

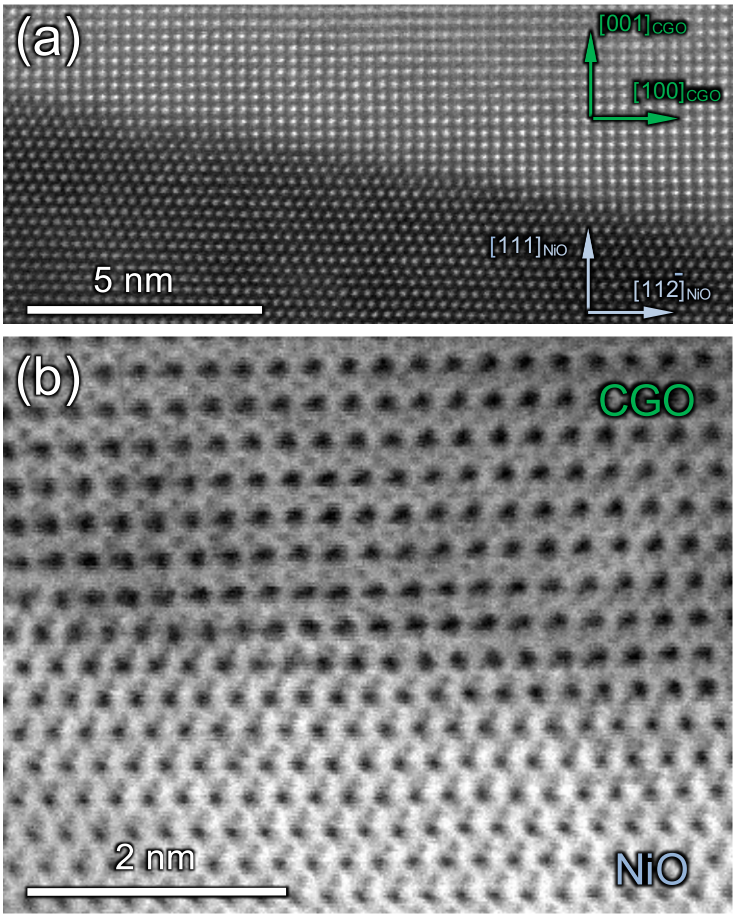

Fig. S3. (a) High Angular Annular Dark Filed (HAADF) STEM image of the NiO-CGO $(001)_{CGO}//(111)_{NiO}$ interface taken along the $[100]_{CGO}//[1\bar{1}0]_{NiO}$ zone axes. (b) Annular Bright Field (ABF) STEM image of the same interface at higher resolution.

2.3.- *Energy Dispersive Spectra (EDS)*

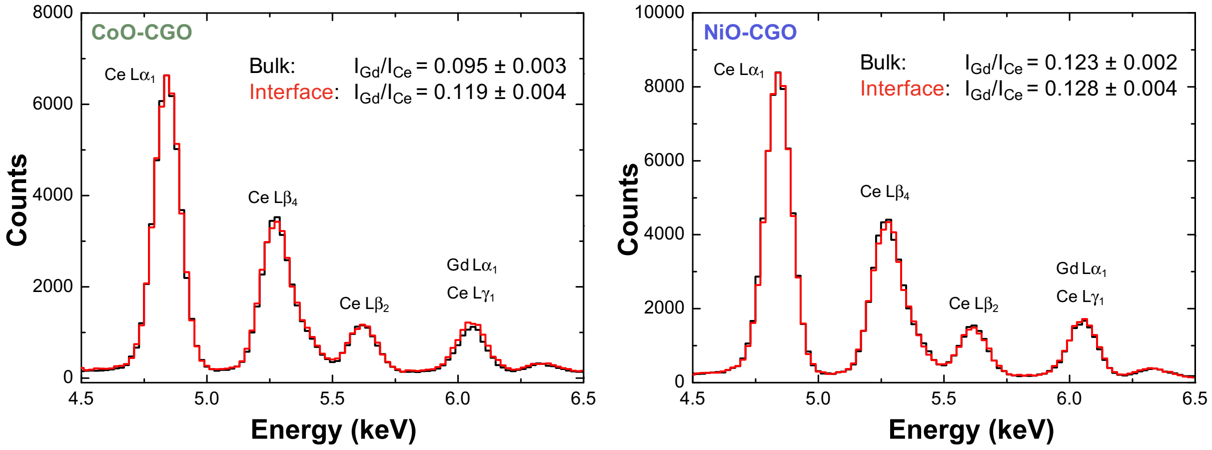

Fig. S4. ED spectra showing the Ce-L and Gd-L X-ray fine structure far from the interface (black) and at the interface (red) for the two type of samples studied. In the CoO-CGO case the intensity of the Ce-Lγ^1 and Gd-Lα^1 overlapping peaks with respect to the adjacent Ce-L left peaks is higher in the spectra taken at the interface, indicating segregation of Gd at the interface. However, this effect is not observed for the NiO-CGO eutectic. The difference between I_{Gd}/I_{Ce} ratios at the interface and at the bulk is $(I_{Gd}/I_{Ce})^{Int} - (I_{Gd}/I_{Ce})^{Bulk} = 0.024 \pm 0.005$. As this value is 4.8σ higher than zero, the probability that both values were compatible is $8\cdot10^{-7}$.[1] However, in the NiO-CGO case we obtain $(I_{Gd}/I_{Ce})^{Int} - (I_{Gd}/I_{Ce})^{Bulk} = 0.005 \pm 0.004$, which means that there is really no difference.

2.4.- *Ce and Co valence states*

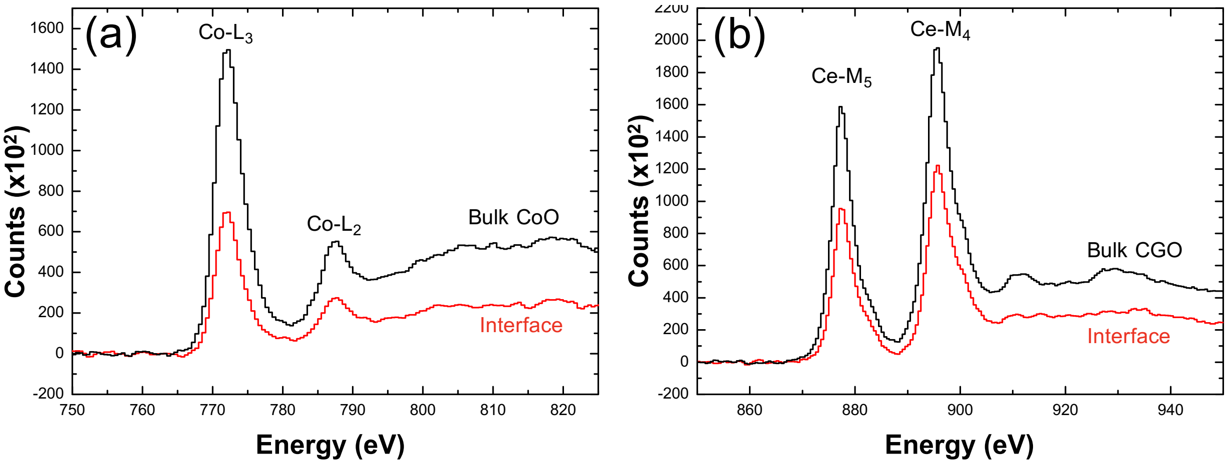

Fig. S5. a) EEL spectra, after background subtraction, of the Co-$L_{2,3}$ lines in bulk CoO (far from the interface) and at the interface. There is no shift in the position of the lines, evidencing that the oxidation state of the Co ions remains predominantly 2+ in the interface region. b) Ce-$M_{5,4}$ edges of the CGO phase in the bulk and at the interface. There are no changes in the position or relative intensities of the Ce-$M_{5,4}$ edges, demonstrating that Ce remains largely 4+.

2.5.- *Elemental profiles by EELS*

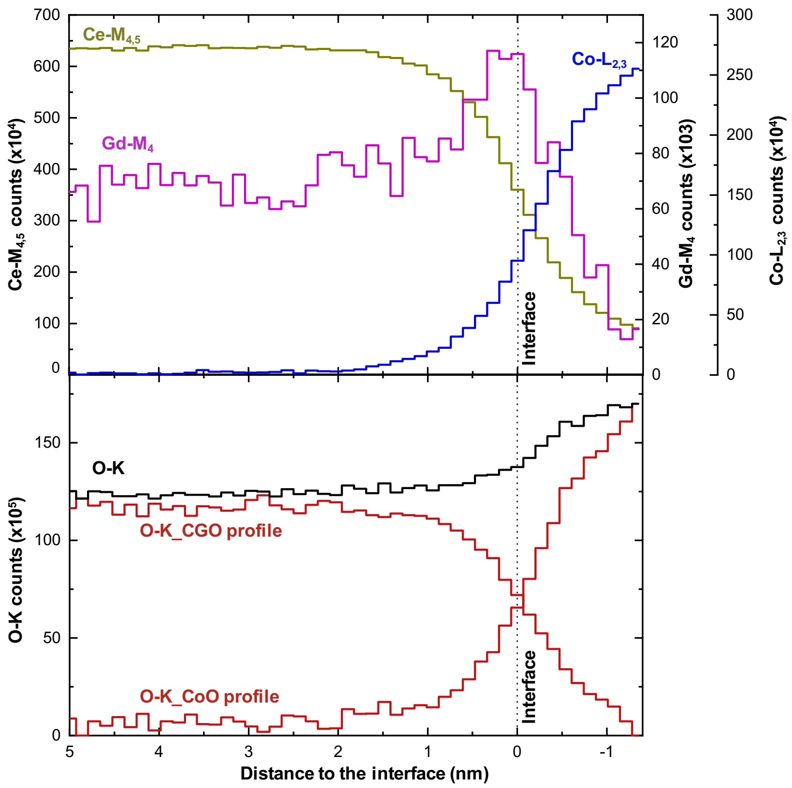

Fig. S6. Top) Cation profiles as a function of the distance to the interface (the position on the interfacial Ce^{4+} and Co^{2+} atomic planes are marked in the graphs). They were obtained by Multiple Linear Least Square (MLLS) fitting using background and signal models extracted from the top pixel of the line-trace (inside the CGO lamella and far from the interface) for Ce-$M_{5,4}$ and Gd-M_4 edges and from the bottom pixel (inside the CoO lamella) for the Co-$L_{2,3}$ edge. Although the Gd-M_4 edge is far less intense than Gd-M_5, the latter overlaps with the Ce-M_3 edge and, consequently, it has not been used for the quantitative analysis. Thus the Gd^{3+} profile is much noisier than the other ones due to its relatively low intensity. Nevertheless, it is clear that the Gd^{3+} concentration increases at the interface.

The Ce and Co chemical profiles are wider than initially expected because they extend on both sides of the interface for about 3-5 unit cells. However, as the HREM images of Figure 2 display very abrupt interfaces between the rock salt and fluorite structure, we think that the profile width is reasonably attributable to the beam broadening produced by the relatively thick STEM specimen (~90 nm). The Co^{2+} and Ni^{2+} signals inside the CGO phase are undetectable far from the interface. This is in good agreement with previous experimental works, considering the fact that small cations like Ni and Co are usually unstable in eightfold coordination,[2, 3] although Chen *et al.* indicated that the solubility of CoO in CeO_2 was ~3 mol% at 1.580 ºC.[4] Nevertheless, the Ce concentration does not tend towards zero inside the Co lamella, as can be observed in the Figure, in good agreement with Chen *et al.,* which also indicated that the CeO_2 concentration in the CoO phase was about 0.5 mol%.

Bottom) Oxygen concentration profiles obtained from MLLS fitting of the EEL spectra. We plot the concentration profiles obtained from fitting to the O-K fine structure to the CGO phase and to the CoO phase (red), as well as the sum of the two contributions (black). For that we used as spectra models, respectively, the top pixel spectrum in the CGO phase and the bottom pixel spectrum in the CoO phase, both after background subtraction, in order to discriminate the contribution from the different phases to the oxygen signal at the interface. The increase in the total O-K signal in CoO phase is attributable to the higher oxygen volume density in CoO (about 5% higher than in CGO) and the higher thickness in this part of the specimen, according to the results of Fig. S1. The ratio between O-K_CGO and Ce+Gd content is already represented in Fig. 4b. The ratio between O-K_CoO and Co is mainly constant in the whole region shown in the figure.

3.- DFT Calculations

3.1 *Bulk CoO and NiO oxides*

CoO and NiO have the rock-salt structure with the $Fm\overline{3}m$ space group. For the bulk of both oxides we considered the AF2 antiferromagnetic state, with parallel spins in the (111) planes, which has been proven to be the ground state.[5] Values of U=5.1 J=1.0 for Co and U=8.0 J=0.95 for Ni *d* orbitals were chosen, these being of the same order as those in earlier studies.[6, 7] A regular Γ−centered 8 × 8 × 8 k-point mesh in the Brillouin zone was used. The calculated lattice parameters are 4.297 Å and 4.184 Å, almost identical to the 4.258Å and 4.179 Å experimental values for CoO and NiO.[8, 9] The band gaps are 2.22 (CoO) and 3.48 (NiO) eV, slightly smaller compared to the experimental 2.6 and 3.8 values,[10, 11] and the atomic spin moment, 2.673 and 1.765 μ_B, which contrast with the 3.35–3.8,[12, 13] and 1.64–1.90,[14-16] previously reported for CoO and NiO, respectively. In the case of CoO, the calculated spin moment is smaller, although its value corresponds to almost three unpaired electrons, which is consistent with a formal Co^{2+} in a high-spin t_{2g}^5 e_g^2 configuration. It has been previously argued that the experimental CoO magnetic moment contains an orbital moment of about 1 μ_B.[17] Fig. S7 represents the density of states for CoO and NiO, with only the DOS corresponding to a metal and one oxygen atom being shown. Furthermore, the ionicity of CoO, as measured by the Bader charges, is almost indistinguishable from NiO.[5]

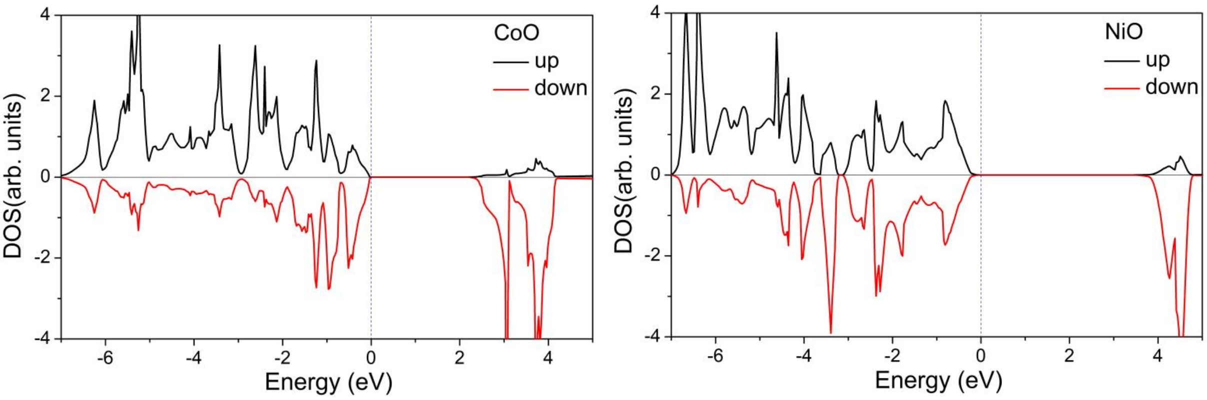

Fig. S7**.** Spin resolved total density of states for the antiferromagnetic CoO and NiO: black lines majority spin and red lines minority spin. In order to show the local moments, only the DOS corresponding to a Co(Ni) and an oxygen in the rock-salt unit cell are represented. The energy zero is located at the top of the valence band.

3.2 *Bulk CeO_2 and Gd-doped CeO_2*

We first considered undoped CeO_2 with the fluorite structure. A 5 x 5 x 5 Monkhorst–Pack k-point mesh for the $Fm\overline{3}m$ fluorite unit cell was applied. As shown in Fig. S8, which shows the calculated density of states within the PBE approximation, we obtained a band gap of about 2 eV, too small as compared with the 6 eV experimental value.[18] As is well known, the DFT method strongly underestimates the band gaps, therefore, we have included a Hubbard-like U parameter for the 4*f*-orbitals of cerium and according to earlier studies a value of 5 eV was chosen.[19, 20] Inclusion of U slightly increases the gap but it is still too small. Nevertheless, the disagreement does not alter our results, since all the investigated systems are insulators. The calculated lattice parameter for the cubic cell a=5.462 Å compares to 5.411 Å experimental value and is consistent with earlier studies.[20, 21]

Next we considered a 2 x 2 x 2 supercell containing 32 Ce and 64 oxygens and placed two Gd atoms in two Ce positions and an oxygen vacancy V_O. The $2Gd_{Ce}$-V_O complex models a neutral defect and corresponds to 6.25 % Gd fraction. A large supercell is used in order to eliminate interactions between complexes. We identified several nonequivalent configurations of Gd and V_O differing in the gadolinium and vacancy relative positions. The energy of the $2Gd_{Ce}$-V_O complex, i.e. the association energies between Gd ions and oxygen vacancies, were calculated for nearest (1NN) and next nearest neighbor (2NN) positions of the vacancy to the Gd. All the complexes show an attractive interaction, as expected from electrostatics, considering the opposite relative charges of Gd ions and oxygen vacancies. In agreement with previous calculations, we found that the 1NN is preferred over the 2NN position and the complex energy decays rapidly with the Gd-V_O distance.[20] All the 1NN configurations have similar energy, the largest difference between two configurations being of ~80 meV. The association energy is not only dependent on the Coulomb interaction, but it is also strongly influenced by elastic effects as previously found.[20, 21] Calculations with a larger 12.5 % Gd fraction yield similar results.

The structure is insulating and non-magnetic and the gap significantly increases with respect to the pure ceria gap, see Fig. S8. Calculations performed without an oxygen vacancy, and only with the Gd dopants, induce defect states in the gap and the system becomes metallic.

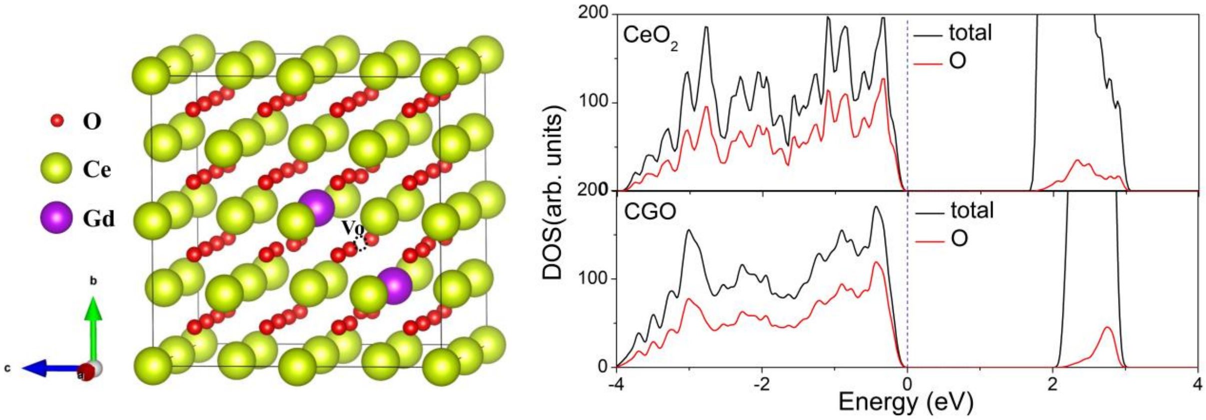

Fig. S8. Atomic positions for the lowest energy configuration of a 2Gd-V_O defect complex in the CeO_2 bulk, the V_O is 1NN to the Gd (left). Total density of states for CeO_2 and Gd-doped CeO_2 (right). Compared to the ideal CeO_2 structure, Ce as well as Gd relax away from the V_O increasing the distance by 0.12 Å regardless of the ion, whereas oxygen atoms move closer to V_O by between 0.27 and 0.35 Å. Defects only affect the local surrounding while the total cell volume is almost constant. Therefore, Gd doping does not change the lattice parameter perceptibly.

3.3 *CGO-CoO and CGO-NiO interfaces*

The interface model was obtained by joining two films, a $(001)_{CeO2}$ and a $(111)_{XO}$, X= Co or Ni, with the structure of the bulk material, aligning the $[010]_{CeO2}//[1\bar{1}0]_{XO}$ and $[100]_{CeO2}//[11\bar{2}]_{XO}$ crystallographic directions. The in-plane unit cell (u.c.) corresponds to a 2 x 2 CeO_2 and a 4 x 4 XO in plane coincident cells. We performed calculations for both, superlattices (SL) with periodic boundary conditions and slabs with two free surfaces, one of CeO_2 and the other one of XO. The SL and slab u.c. contains 20 atomic layers, 10 of CeO_2 and 10 of XO. The SL has two equal interfaces, while the slab presents two polar free surfaces, one of cerium and the other one of oxygen. In both types of calculations the two oxides were stoichiometric. We performed calculations for the in-plane lattice parameter of CGO and the XO slabs inhomogeneously deformed to match the fluorite structure of the (001), therefore they undergo a compression strain of 8.9 and 3.6 % for the CoO and NiO, respectively. We also performed calculations in which the CGO is under uniform tensile strain to match the equilibrium u.c. area of the transition metal oxides. This entails an expansion of the CGO lattice parameter of 4.4 and 1.6 % for the CGO-CoO and CGO-NiO interfaces, respectively. In the initial structures the atomic positions of the unstrained oxides were fixed to those of the bulk, while in the strained oxide they are proportional to the unit cell deformation. Full structural optimization was always performed to obtain the out-of-plane *c*–axis lattice constant, as well as the internal atomic positions within the cell.

The results presented in the main text correspond to those of the SL with periodic boundary conditions. The qualitative picture obtained with the slab calculations is equivalent, although the total energies were indeed different due to the contribution from the free surfaces in the slab calculations. In fact, in the case of the slab, the segregation energy for the CGO-NiO is negative, indicating that in this case $2Gd_{Ce}$-V_O should preferably be located in the center of the slab. However, since the surface relaxation also contributes to the total energy of the slab, we consider that the SL models describe the experimental systems more accurately. In addition, the interfaces in which the CeO_2 is under tensile strain present a slightly smaller strength for both systems, although the qualitative picture is identical.

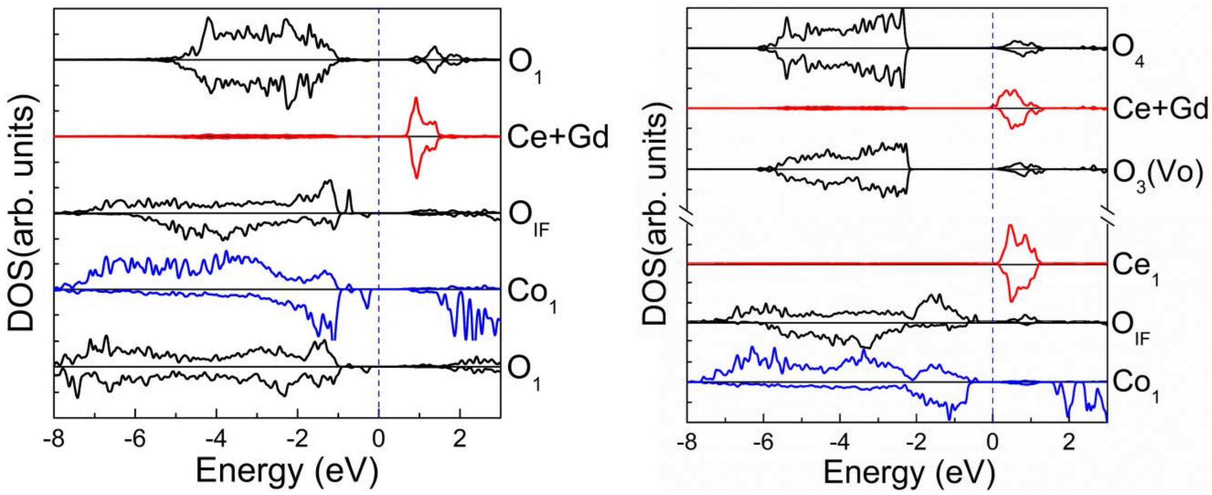

Fig. S9. Atomic plane projected spin-resolved density of states of the CeO_2-CoO systems containing the $2Gd_{Ce}$-V_O complex at the interface (left) and in the center of the CeO_2 slab (right). On the left panel only the interface O_{IF} and nearest neighbor planes are displayed, while on the right panel the planes around the $2Gd_{Ce}$-V_O complex and those at the interface are shown. The upper and lower lines within each plane represent the majority and minority spin-density, respectively. Energy zero is located within the gap which, although small, is absolute and maintained in all the planes for both systems.

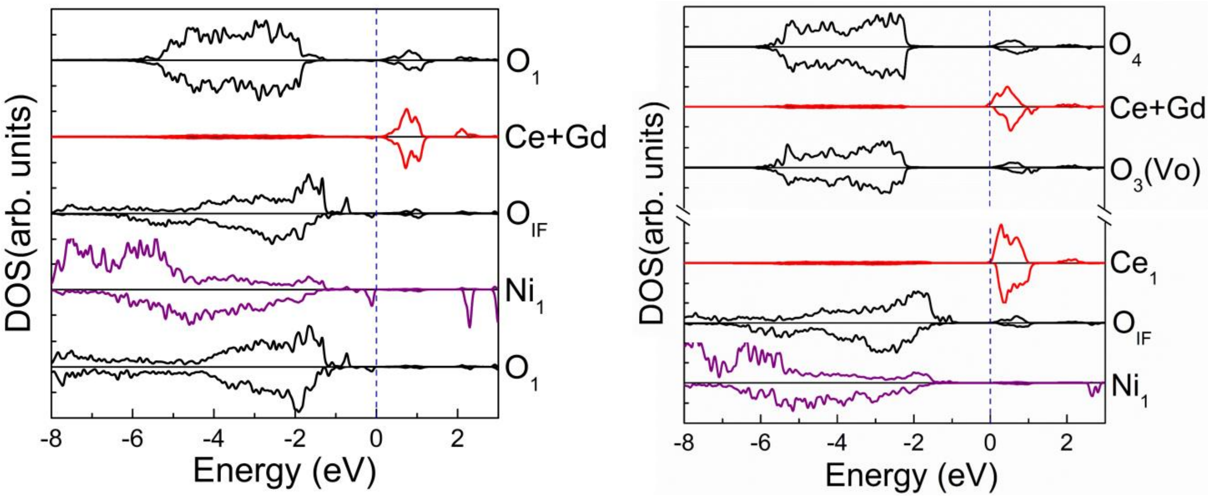

Fig. S10. Same as Figure S9 for the CeO_2-NiO systems with the $2Gd_{Ce}$-V_O complex at the interface (left) and in the center of the CeO_2 slab (right).

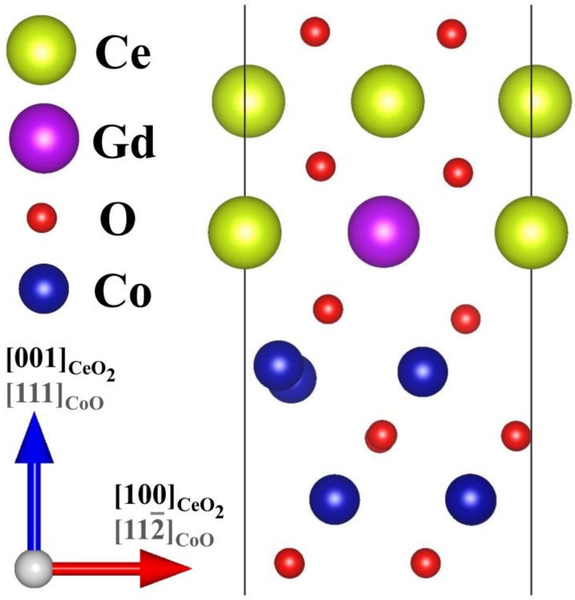

Fig. S11. Lateral view of the interface planes for the CeO_2-CoO systems with the $2Gd_{Ce}$-V_O complex at the interface. The atoms are at the positions obtained in the relaxed DFT calculations.

References

1. P. R. Bevington and D. K. Robinson, *Data reduction and Error Analysis for the Physical Sciences*, McGraw-Hill Higher Education, 3rd edn., 2003.
2. J. Ranlov, F. W. Poulsen and M. Mogensen, *Solid State Ionics*, 1993, **61**, 277.
3. L. Ortega-San-Martin, J. I. Pena, A. Larrea and V. M. Orera, *J. Eur. Ceram. Soc.*, 2011, **31**, 1269.
4. M. Chen, B. Hallstedt, A. N. Grundy and L. J. Gauckler, *J. Am. Ceram. Soc.*, 2003, **86**, 1567.
5. T. Bredow and A. R. Gerson, *Phys. Rev. B*, 2000, **61**, 5194.
6. T. Archer, R. Hanafin and S. Sanvito, *Phys. Rev. B*, 2008, **78**, 014431.
7. H. X. Deng, J. B. Li, S. S. Li, J. B. Xia, A. Walsh and S. H. Wei, *Appl. Phys. Lett.*, 2010, **96**, 162508.
8. M. J. Redman and E. G. Steward, *Nature*, 1962, **193**, 867.
9. D. R. Lide, *CRC Handbook of Chemistry and Physics*, CRC, Boca Raton, FL, 1998/1999.
10. P. A. Cox, *Transition Metal Oxides: An Introduction to Their Electronic Structure and Properties*, Clarendon, London, 1995.
11. F. Parmigiani and L. Sangaletti, *J. Electron Spectroscopy and Related Phenomena*, 1999, **98**, 287.
12. D. C. Khan and R. A. Erickson, *Phys. Rev. B,* 1970, **1**, 2243.
13. D. Herrmann-Ronzaud, P. Burlet and J. Rossat-Mignod, *J. Phys. C-Solid State Phys.*, 1978, **11**, 2123.
14. B. E. F. Fender, A. J. Jacobson and F. A. Wedgwood, *J. Chem. Phys.*, 1968, **48**, 990.
15. H. A. Alperin, *J. Phys. Soc. Jpn. Suppl. B*, 1962, 12.
16. A. K. Cheetham and D. A. O. Hope, *Phys. Rev. B*, 1983, **27**, 6964.
17. J. Hugel and M. Kamal, *Solid State Comm.*, 1996, **100**, 457.
18. E. Wuilloud, B. Delley, W. D. Schneider and Y. Baer, *Phys. Rev. Lett.*, 1984, **53**, 202.
19. J. Paier, C. Penschke and J. Sauer, *Chem. Rev.*, 2013, **113**, 3949.
20. S. Grieshammer, T. Zacherle and M. Martin, *Phys. Chem. Chem. Phys.*, 2013, **15**, 15935.
21. D. A. Andersson, S. I. Simak, N. V. Skorodumova, I. A. Abrikosov and B. Johansson, *P Natl Acad Sci USA*, 2006, **103**, 3518.